

ARTICLE OPEN



Wireless, multimodal sensors for continuous measurement of pressure, temperature, and hydration of patients in wheelchair

Seokjoo Cho¹, Hyeonseok Han¹, Hyunwoo Park², Sung-Uk Lee³, Jae-Hwan Kim⁴, Sung Woo Jeon⁴, Mengqiu Wang⁵, Raudel Avila⁶, Zhaoqian Xi^{5,7,8}, Kabseok Ko⁹, Minsu Park¹⁰, Jungyup Lee¹¹, Myungwoo Choi¹², Je-Sang Lee¹³, Weon Gi Min¹⁴, Byeong-Ju Lee¹⁵, Soyeong Lee¹⁶, Junrak Choi¹, Jimin Gu¹, Jaeho Park¹, Min Seong Kim¹, Junseong Ahn¹, Osman Gul¹, Chankyu Han¹, Gihun Lee¹, Seunghwan Kim¹, Kyuyoung Kim¹, Jeonghyun Kim¹⁷, Chang-Mo Kang¹⁸, Jahyun Koo^{19,20}, Sung Soo Kwak²¹, Sungbong Kim²², Dong Yun Choi²³, Seokwoo Jeon¹², Hyung Jin Sung¹, Yong Bae Park^{16,24}, Minkyu Je², Young Tae Cho²⁵, Yong Suk Oh²⁵✉ and Inkyu Park¹✉

Individuals who are unable to walk independently spend most of the day in a wheelchair. This population is at high risk for developing pressure injuries caused by sitting. However, early diagnosis and prevention of these injuries still remain challenging. Herein, we introduce battery-free, wireless, multimodal sensors and a movable system for continuous measurement of pressure, temperature, and hydration at skin interfaces. The device design includes a crack-activated pressure sensor with nanoscale encapsulations for enhanced sensitivity, a temperature sensor for measuring skin temperature, and a galvanic skin response sensor for measuring skin hydration levels. The movable system enables power harvesting, and data communication to multiple wireless devices mounted at skin-cushion interfaces of wheelchair users over full body coverage. Experimental evaluations and numerical simulations of the devices, together with clinical trials for wheelchair patients, demonstrate the feasibility and stability of the sensor system for preventing pressure injuries caused by sitting.

npj Flexible Electronics (2023)7:8; <https://doi.org/10.1038/s41528-023-00238-3>

INTRODUCTION

Pressure injuries are localized damage to the skin or underlying tissues caused by prolonged pressure over bony prominences, deteriorated by increased skin temperature and hydration level^{1,2}. These pressure injuries usually occur in patients with reduced mobility confined to wheelchairs and beds for long periods^{3,4}. In general clinically relevant range of pressure injury is known as a prolonged pressure (~10 kPa) of the skin-mattress interface for patient lying in bed⁵. However, there is a lack of clinical indicators for the occurrence of sitting acquired injuries according to various health conditions, such as weight and degree of paralysis. Patients in a wheelchair are vulnerable to pressure injuries caused by sitting since more than 50% of their body weight is applied to 8% of the body surface area, including the ischial tuberosities, heels, posterior thighs, and scapulae⁶. In particular, spinal cord injury (SCI) patients who use wheelchairs for transportation have a very high risk of developing the pressure injuries caused by sitting due

to unawareness of the pressure overload^{7,8}. The maximum pressure between the wheelchair mattress and paraplegic patients are reported over the 100 kPa, depending on the interface of the skin-mattress^{7,9,10}. Other complications and health conditions such as hemiplegia and spasticity can cause unbalanced posture of the sitting patients and pressure concentration of specific bony prominence. (Supplementary Note 1) An estimated 46,000 SCI patients in the United States suffer from pressure injuries, and the corresponding treatment costs \$1.2 billion annually¹¹. As pressure injuries significantly lowers the health-related quality of life of patients and increases the economic burdens associated with medical treatment, prevention of these injuries at an early stage is of critical importance^{12–16}. In general, clinical practice guidelines for the prevention of pressure injuries caused by sitting, recommended by the National Pressure Injury Advisory Panel (NPIAP), involve repositioning (e.g., pushing up and holding the armrest) for pressure relief at regular intervals for wheelchair

¹Department of Mechanical Engineering, Korea Advanced Institute of Science and Technology, Daejeon 34141, Republic of Korea. ²School of Electrical Engineering, Korea Advanced Institute of Science and Technology, Daejeon 34141, Republic of Korea. ³Advanced 3D Printing Technology Development Division, Korea Atomic Energy Research Institute, Daejeon 34057, Republic of Korea. ⁴Department of Electrical and Computer Engineering, University of Illinois at Urbana-Champaign, Urbana, IL 61801, USA. ⁵State Key Laboratory of Structural Analysis for Industrial Equipment, Department of Engineering Mechanics, Dalian University of Technology, Dalian 116023, P. R. China. ⁶Department of Mechanical Engineering, Northwestern University, Evanston, IL 60208, USA. ⁷DUT-BSU Joint Institute, Dalian University of Technology, Dalian 116023, China. ⁸Ningbo Institute of Dalian University of Technology, Ningbo 315016, China. ⁹Department of Electronics Engineering, Kangwon National University, Chuncheon 24341, Republic of Korea. ¹⁰Querrey-Simpson Institute for Bioelectronics, Northwestern University, Evanston, IL 60208, USA. ¹¹Sibel Health Inc, Niles, IL 60714, USA. ¹²Department of Materials Science and Engineering, KAIST Institute for The Nanocentury (KINC), Korea Advanced Institute of Science and Technology, Daejeon 34141, Republic of Korea. ¹³Department of Rehabilitation Medicine, Gimhae Hansol Rehabilitation & Convalescent Hospital, Gimhae 50924, Republic of Korea. ¹⁴Department of planning and development, Gimhae Hansol Rehabilitation & Convalescent Hospital, Gimhae 50924, Republic of Korea. ¹⁵Department of rehabilitation medicine, Pusan national university hospital, Busan 49241, Republic of Korea. ¹⁶Department of AI Convergence Network, Ajou University, Suwon 16499, Republic of Korea. ¹⁷Department of Electronic Convergence Engineering, Kwangwoon University, Seoul 01897, Republic of Korea. ¹⁸Korea Photonics Technology Institute, Gwangju 61007, Republic of Korea. ¹⁹School of Biomedical Engineering, Korea University, Seoul 02841, Republic of Korea. ²⁰Interdisciplinary Program in Precision Public Health, Korea University, Seoul 02841, Republic of Korea. ²¹Center for Bionics of Biomedical Research Institute, Korea Institute of Science and Technology, Seoul 02792, Republic of Korea. ²²Department of Chemistry, Korea Military Academy, Seoul 01805, Republic of Korea. ²³Biomedical Manufacturing Technology Center, Korea Institute of Industrial Technology (KITECH), Yeongcheon 38822, Republic of Korea. ²⁴Department of Electrical and Computer Engineering, Ajou University, Suwon 16499, Republic of Korea. ²⁵Department of Mechanical Engineering, Changwon National University, Changwon 51140, South Korea.

✉email: oyongsuk@changwon.ac.kr; inkyu@kaist.ac.kr

users^{17–19}. However, these approaches are insufficient to prevent the formation of pressure injuries caused by sitting completely and systematically. Therefore, there is a need for technologies that support patients or caregivers by continuously measuring pressure at critical locations and providing alerts regarding the need for repositioning while moving in a wheelchair or stationary. In addition, continuous measurement of the skin temperature and hydration level are helpful for preventing pressure injuries^{1,2,20,21}. Skin temperature provides a physiological indicator to prevent skin breakdown since the tissue metabolism becomes more active at higher temperature²¹. Also, high level of hydration induces the friction-induced damage by increasing the coefficient of friction at skin-mattress interfaces¹.

Recent advances in technologies for continuous measurement of physical or physiological signals at skin interfaces of individuals support a quantitative approach to evaluating the risk of pressure injury formation. Previous reports suggest multiple pressure sensors embedded in the cushion of a wheelchair for pressure mapping under changes in posture^{6,22–24}. However, these technologies do not simultaneously track ulcer-related variables, including pressure, temperature, and skin hydration, at the locations of interest vulnerable to pressure injuries. On the other hand, several studies introduce skin-mountable sensors, characterized by their thin, flexible, and lightweight properties, which enable continuous monitoring of pressure and temperature^{25–28}. These sensors integrated with wireless platforms have considerable potential for continuous measurement of pressure and temperature from the skin in contact with various media, including bed mattresses^{25,26}, prosthetic sockets²⁷, and therapeutic compression garments²⁸. In addition, a few reports suggest various methods for measuring the skin hydration level using galvanic skin response (GSR)^{29,30}. However, it has not been reported yet to simultaneously measure pressure, temperature, and hydration at skin interfaces.

For the prevention of disease occurrence of paraplegic patients, previous studies proposed the wheelchair based sensing system that capable of pressure^{23,31,32}, temperature^{33–35} and galvanic skin response(GSR)³⁶ monitoring of wheelchair patients. However, those studies are limited to a signal monitoring for a single ulcer related parameter, without clinical trials on wheelchair patients. In addition, many patients using wheelchairs have activities, such as moving in and out of the hospital, but previous studies have limitations in that readout system are not integrated with wheelchairs, thereby reducing the mobility of wheelchair patients. Therefore, movable sensing system integrated with wheelchair that provides that provides multimodal capabilities for continuous, simultaneous measurement of various ulcer-related variables is important for early diagnosis and prevention of pressure injuries.

As the rigid, bulk form factor of the device lead to unwanted damages of skin, the pressure sensor essentially needs a design of soft, thin, and small-sized form for use in various applications considered here. In addition, piezoresistive pressure sensors based on a variety of conductive materials, including silicon membranes^{26,37–39}, metal films^{25,27,28}, liquid metals^{40–44}, graphene^{45–47}, and carbon nanotubes^{48–50} support easy integration with battery-free, wireless platforms owing to their simple device design and readout circuit. In particular, the typical metal films support the formation of relatively reliable, repeatable pressure sensors. However, the intrinsically low sensitivity of metal films (a yield strain <0.3%) hinders their pressure-sensing capability over a wide range of pressures for use in various applications. One of the few possible means of resolving this issue is the use of nanoscale crack junctions, fabricated using fatigue or cyclic loading of metal films, which significantly increases the response to loadings^{51–53}. In addition, recent studies suggest that encapsulation layers, including polyimide (PI)⁵⁴, polydimethylsiloxane (PDMS)⁵⁵, and self-healing polymer⁵⁶ can improve the stability and repeatability issues arising from the low robustness of metal films.

As an advanced technology of the previously reported sensor systems^{25,26} (see Supplementary Table 1), we introduce a battery-free, wireless, skin-mountable, multimodal sensors and a movable system for continuous monitoring of pressure, temperature, and hydration at skin interfaces of patients on wheelchairs. The device design includes the crack-activated pressure sensor with nanoscale encapsulations that shows enhanced sensitivity and robustness at pressures below 100 kPa caused by sitting, along with insensitivity to bending and shear forces. Crack-activated pressure sensor with a nanoscale encapsulation can provide not only high resistance change ($\Delta R/R_0 = 2.5\%$ @ 100 kPa), but also high linearity, low hysteresis, and long-term ability that are similar with those of conventional Au film as shown in Supplementary Table 2. In addition, this device supports simultaneous measurement of skin temperature and hydration level caused by sweat generation at mounting locations of the device. Benchtop studies demonstrate the sensing performances of the device, verified by numerical simulations. The movable sensing system combined with the four multiplexed antennas enables accurate, repeatable, and continuous measurement of pressure, temperature, and hydration by the multiple sensors mounted at critical locations of subjects sitting in wheelchairs while stationary or in motion. Experiment results and numerical simulations of movable system demonstrate not only the practical utility, but also functional characterization of this system. Experimental evaluation includes measuring the maximum operating distance, runtime, and signal monitoring with outside sidewalks using movable sensing system. A clinical trial with SCI patients in wheelchairs, along with weight shifting behavior for pressure relief, demonstrates the feasibility and stability of the battery-free, wireless sensor and movable system.

RESULTS

Battery-free, wireless, skin-mountable sensing platform and movable system

Figure 1a provides a schematic illustration of the movable sensing system integrated with a wheelchair, which consists of primary antennas, a multiplexer, a near field communication (NFC) reader, portable batteries, and portable devices (a notebook and a smartphone) to provide power delivery and data communication with the sensors at the skin interfaces of the subject while stationary or moving. Figure 1b, c shows a schematic illustration and a photograph of the battery-free, wireless sensing platform that includes an NFC system-on-a-chip (SoC), electronic components, a Wheatstone bridge, an instrumentation amplifier, and a receiver antenna, connected via serpentine interconnects to a crack-activated pressure sensor, a negative temperature coefficient (NTC) thermistor as a temperature sensor on the front side of a flexible printed circuit board (PCB) and two metal pads as the GSR sensor on its back side. The NFC reader transfers the power to drive the designed circuit to readout data from pressure, temperature, and GSR sensors through the receiver antenna using resonant magnetic inductive coupling. The Wheatstone bridge and two voltage dividers convert a change in resistance of the pressure, temperature, and GSR sensors into a change in voltage, respectively. For pressure sensor, the change in voltage passes the instrumentation amplifier for amplifying the signal to improve the signal quality (Supplementary Fig. 1). The internal analog-to-digital converter (ADC) in the NFC SoC converts the voltage signals obtained from the pressure, temperature, and GSR sensors into digital signals in turn. Finally, the NFC SoC converts the digital signals into a data format conforming to the ISO 15693 protocol and transfers the data to the NFC reader. Figure 1d illustrates the overall operation as a block diagram of the functional components. Figure 1e(i) provides photographs of the subject sitting in the wheelchair and the mounting locations of devices. Figure 1e(ii, iii) presents photographs of the device mounted on the posterior

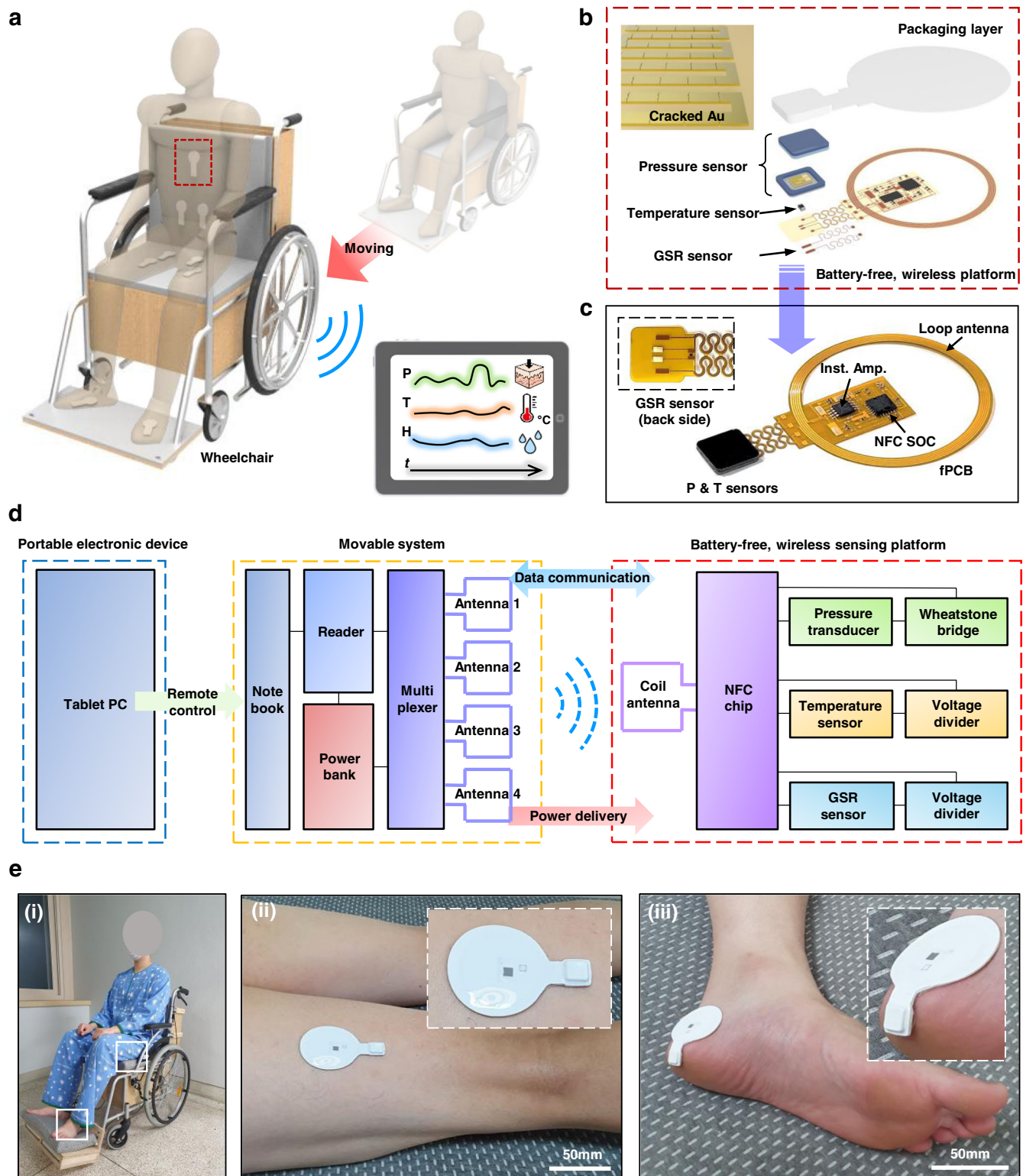
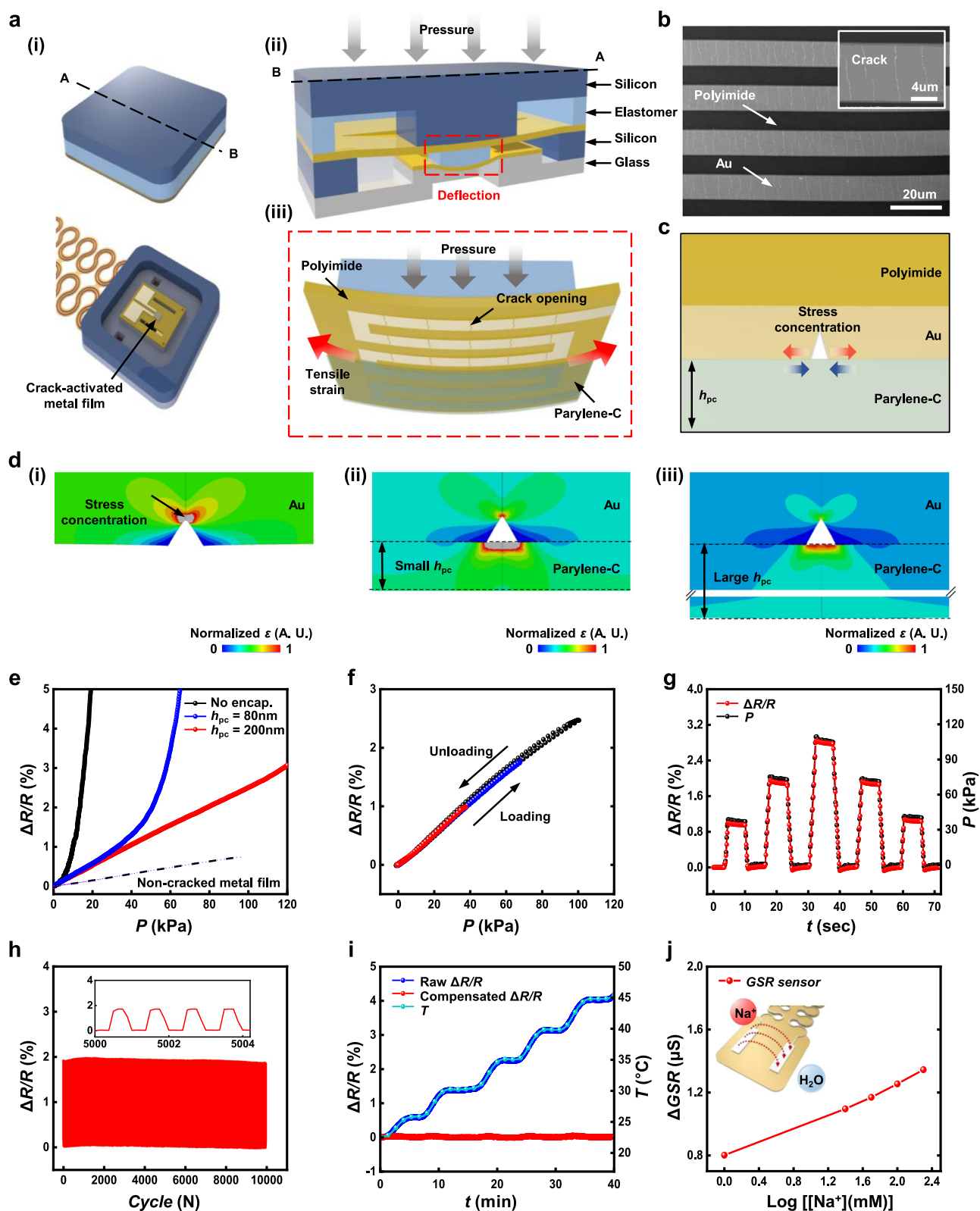


Fig. 1 Schematic illustrations, photographs, and overview of battery-free, wireless sensing platform and movable system. **a** Schematic illustration of the movable system. **b** Schematic illustration of the battery-free, wireless sensing platform that includes crack-activated pressure sensor, temperature sensor, and GSR sensor. **c** Photograph of the sensing platform. Inset shows the GSR sensor located at the back side of flexible PCB. **d** Block diagram of the overall system. **e** (i) Photographs of the subject sitting on a wheelchair. Photograph of the devices mounted at two mounting locations, including (ii) Posterior thighs. (iii) Heel.

thighs and heels that are high-risk regions for developing the pressure injuries caused by sitting. The thin, soft PDMS packaging of the device mechanically and electrically protects the electronics from biofluids and prevents the device from damaging skin.

(Supplementary Fig. 2) In addition, a serpentine interconnector between the multimodal sensors and NFC SoC/receiver coil supports conformal contact of the multimodal sensor to the curved skin and stable detection of signals even under postural



change. Supplementary Fig. 3 illustrates the structural design of the platform used to obtain reversible responses from finite element analysis (FEA) results for stretching and bending. These results indicate that the device ensures gentle placement on the curved skin without mechanical or electrical failure, even under change in posture.

Design and mechanism of the multi-modal sensor

Figure 2a(i–iii) presents schematic illustrations of the design and sensing mechanism of the crack-activated pressure sensor that includes a tri-layered film (PI film/cracked Au/Parylene-C, 75 μm/0.03 μm/0.2 μm in thickness) to obtain enhanced sensitivity as well as low hysteresis and minimal drift at pressures of <100 kPa.

Fig. 2 Schematic illustrations and performance characteristics of multi-modal sensor. **a** Schematic illustration of pressure sensor. (i) Extended view schematic of sensor. (ii) Operating mechanism of the pressure sensor. (iii) Crack-activation of Au metal film. **b** SEM image of crack-activated metal film. **c** Crack opening of metal film with Parylene-C encapsulation layer. **d** (i–iii) FEA results for strain distribution on the cracked metals with different thicknesses of the encapsulation. **e** Fractional changes in the resistances of cracked metal films with two different thicknesses of the encapsulation layer, a cracked metal film with no encapsulation layer, and a non-cracked metal film. **f** Reversible responses of the cracked metal film under loading and releasing. **g** Fractional change in resistance of cracked metal film under different cyclic loading/unloading. **h** Fractional change in resistance of cracked metal film against 10,000 cyclic loadings. Inset shows fractional change in resistance around 5000 cycles. **i** Temperature compensation for cracked-activated pressure sensor for different temperature changes. **j** Fractional change in conductance at different Sodium Chloride concentration.

The “Assembly of the pressure sensor” subsection of the “Methods”, Supplementary Fig. 4 describe the design and key materials used to fabricate the crack-activated pressure sensor. The applied pressure deforms the soft frame and deflects the membrane film, enabling bending of the tri-layered film. The soft frame functions to control the operating range of the pressure sensor by modulating the effective modulus of the sensor as shown in Supplementary Fig. 5 and Supplementary Note 2. This bending of the tri-layered film leads to tensile strain in the cracked Au trace, as an active layer located under the neutral axis, significantly increasing the fractional change in resistance due to crack openings, compared to those of typically evaporated metals without cracks. Figure 2b shows a scanning electron microscope image of the cracked Au traces (Cr/Au, 10 nm/30 nm in thickness) on the PI film, which depend on the repeated pre-stretching, as shown in Supplementary Fig. 6. Supplementary Fig. 7 shows the performance of pressure sensor based on the different pre-stretching strains applied to the metal film. The effect of crack is negligible under 2% pre-strain, and pressure sensor shows constant response over 4% pre-stretch strain. Based on these results, 4% pre-stretch strain was chosen to fabricate the cracked metal thin film. Supplementary Fig. 7b shows the initial resistance of the metal film under the different cycling times with 4% pre-strain. The initial resistance of the metal film converged to a constant value ($R_0 \sim 4 \text{ k}\Omega$) after 100 times of pre-stretching. After crack generation of metal film, a nanoscale thin film of Parylene-C acts as an encapsulation layer to protect the cracked Au film from serious damage, and minimizes both the hysteresis and drift. The pressure sensor requires high sensitivity, high linearity, low hysteresis, and minimum drift over the required pressure ranges for the applications considered here. The “Method” section and Supplementary Fig. 8 describe the experimental setup for evaluating the sensing performance. Figure 2c shows a cross-sectional schematic illustration of the tri-layered film subjected to tensile stress under loading. The encapsulation film with nanoscale thickness (h_{pc}) relieves the stress concentration at a cracked region of the metal film. In addition, Fig. 2d presents FEA results for strain distribution in the cracked metal films with no encapsulation, small h_{pc} and large h_{pc} under loadings. These results indicate that the stress concentration at the cracked region of the metal film decreases with increasing h_{pc} . In Supplementary Fig. 9, the cracked Au traces on the PI film without encapsulation show very high sensitivity, although they exhibit high hysteresis and drift. Conversely, the tri-layered films encapsulated with thicknesses of 80 nm and 200 nm show high sensitivity with high linearity at the pressures <40 kPa and <120 kPa, respectively, which are superior to those of a conventional Au film (Fig. 2e). Changing the thickness of Parylene-C revealed a trade-off between sensitivity and stability (Supplementary Fig. 10). Supplementary Fig. 11a shows the response of the crack-activated pressure sensor with different thickness of parylene-C encapsulation (h_{pc}) under 100 kPa. These results indicate that the sensitivity of the pressure sensor decreased with increasing h_{pc} . Supplementary Fig. 11b shows that linearity of the response of pressure sensor with parylene-C encapsulation ($h_{pc} = 200 \text{ nm}$) maintained over the target pressure range ($\sim 100 \text{ kPa}$). Supplementary Fig. 11c

compares the fractional changes in the resistance of the crack-activated pressure sensor under different pre-deflection, which depends on the thickness of the rigid pad from 250 μm to 300 μm . These results indicate that adjusting the pre-deflection significantly increases in the fractional change in the resistance of the pressure sensor. Figure 2f exhibits perfectly reversible responses against three different loadings of 40, 70, and 100 kPa with negligible hysteresis (<0.01%). Figure 2g summarizes the fractional changes in resistance against the applied pressure during three cyclic loadings and unloadings (rate of $1 \mu\text{m s}^{-1}$; sampling rate of 5 Hz). These changes vary with stepwise loadings (40, 70, and 100 kPa) and return to their initial values with negligible drift (<0.06%) after unloading Fig. 2h shows the long-term stability and mechanical durability under 10,000 cyclic loadings of 80 kPa. The inset depicts the responses after 5000 cyclic loadings with negligible drift (<0.01%) in the signals and no damage to the device. Supplementary Fig. 12 shows the initial resistance of pressure sensor before and after the cyclic loading. The average initial resistance of pressure sensor before the cycle loading is 2917.2Ω (standard deviation = 0.122Ω). After cycle loading, the average resistance of pressure sensor is 2917.7Ω (standard deviation = 0.033Ω). The fractional change in the initial resistance is only 0.02%, indicating the negligible change in initial resistance. In addition, Supplementary Fig. 11d exhibits high sensor-to-sensor uniformities (relative standard deviation = 2.48%) in the pressure regime of <100 kPa. The device shows good recoverability for the repeated loading/unloading under 100 kPa, as shown in Supplementary Fig. 11e. Supplementary Fig. 11f shows a stable and constant response under a constant step load of 60 kPa for 1 h, confirming the ability to accurately measure sustained pressures for prolonged periods of time. The resistivity of the cracked Au trace is temperature-dependent. Figure 2i presents the raw and compensated responses of the crack-activated pressure sensor under various temperature changes. These results indicate that the effect of temperature on the cracked Au traces can be eliminated using temperature data measured from the NTC thermistor and calibration equation, as shown in Supplementary Fig. 13. In addition, Fig. 2 shows the responses of the GSR sensor to different concentrations of sodium chloride as an electrolyte. The results present the high linearity between the GSR value measured using the GSR sensor and log-transformed concentration of the sodium chloride. Supplementary Fig. 14a shows comparison of measured GSR values with data obtained using a commercial, electronic device (IC-HSC001, Innosight) based on bioelectrical impedance analysis, generally used as a gold standard⁵⁷, at various mounting locations of device, including spinous process, sacrum, thigh, and heel. Supplementary Fig. 14b presents a relationship between the GSR and commercial hydration sensor. These results indicate that GSR values can be used as an indicator to measure relative changes in the skin hydration level. Supplementary Fig. 14c shows that the skin hydration level during sweat generation returns to an initial value according to sweat evaporation. This result indicates that the GSR sensor supports continuous monitoring of the skin hydration level caused by sweat generation and evaporation.

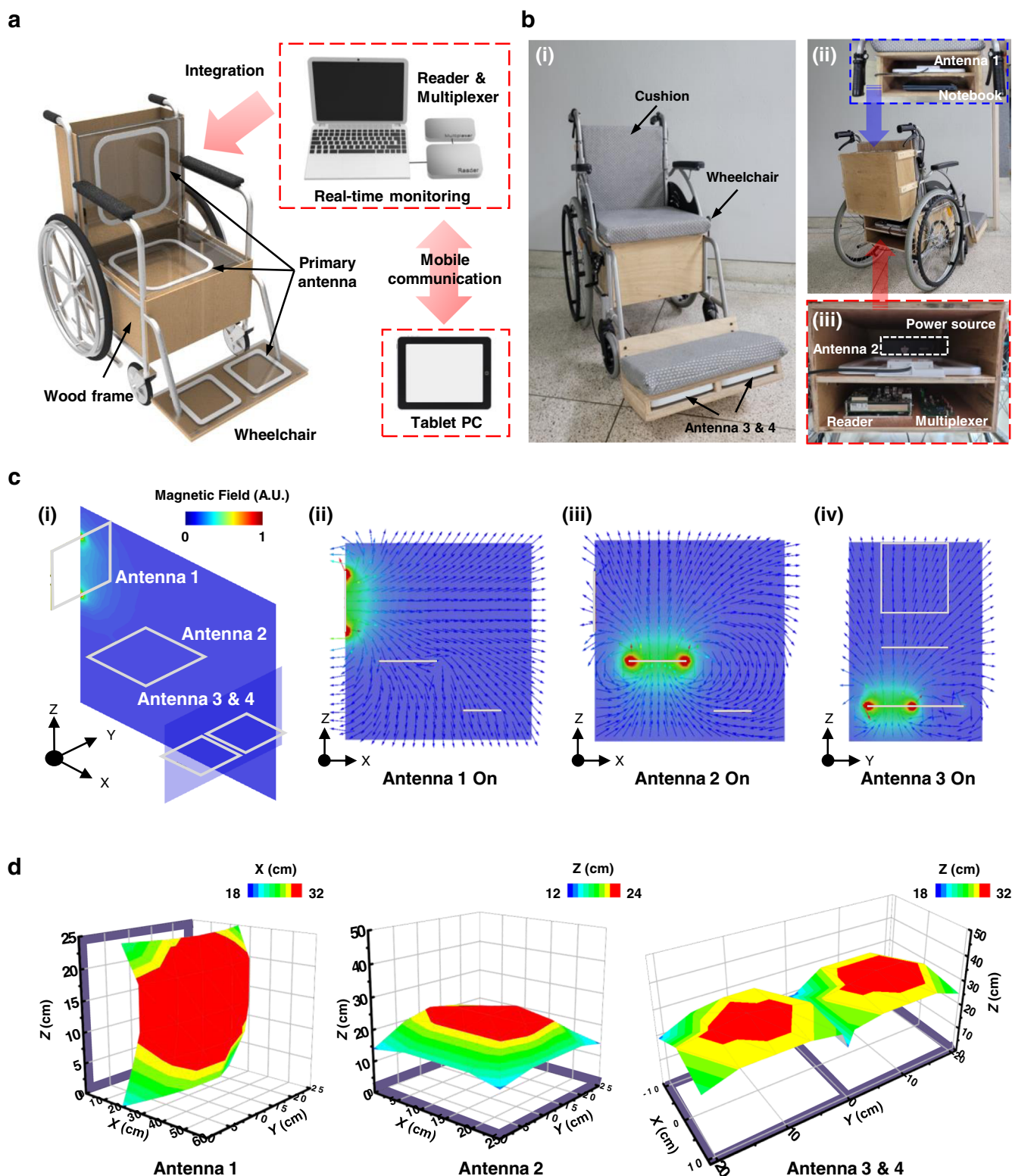


Fig. 3 Schematic illustrations and photographs of battery-free, wireless, movable sensing system. **a** Schematic illustration of the overall system integrated with a wheelchair. **b** Photographs of the movable system, including four primary antennas; multiplexer; antenna reader; notebook for real-time monitoring. **c** Magnetic field distribution for multiplexed antenna configuration. **d** Experimental measurements of operating range for the four multiplexed antennas.

Multiplexed antenna integrated with the wheelchair

Figure 3a, b presents a schematic illustration and photographs of the movable sensing system for continuous monitoring of pressure, temperature, and hydration across many locations at

interfaces between the skin and cushions for a subject sitting in a wheelchair. The system consists of four multiplexed antennas (antenna 1, behind the backrest; antenna 2, below the seat; and antennas 3 and 4, below the footrest) to provide full-body

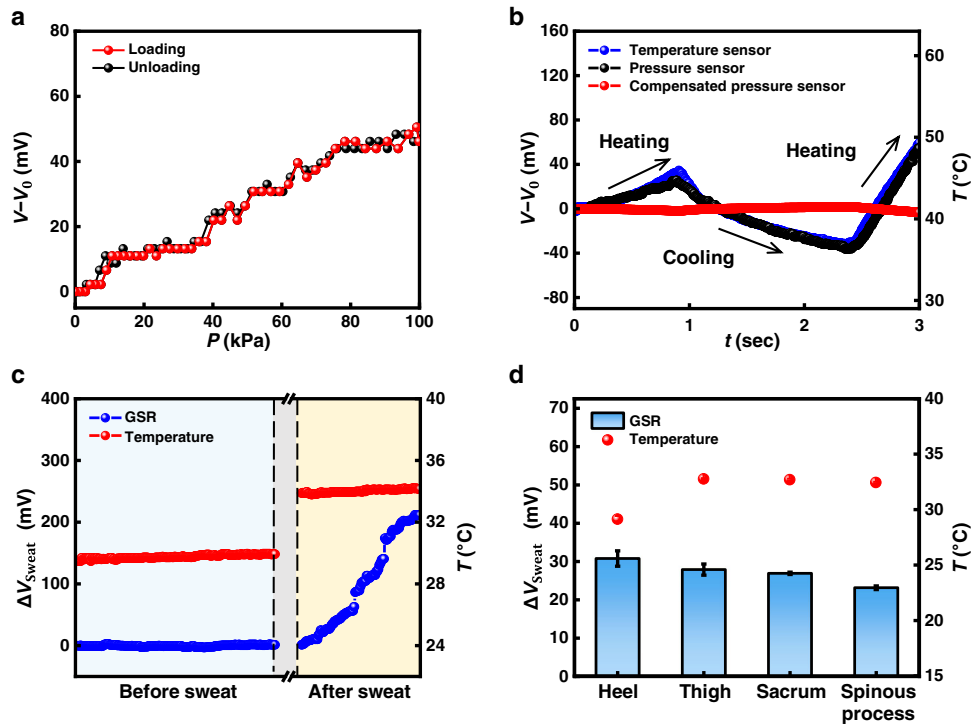


Fig. 4 Performance characteristics of battery-free, wireless multi-modal sensor. **a** Change in the measured voltage of the pressure sensor under 100 kPa loading/unloading. **b** Change in the measured voltage of the pressure sensor by temperature variation (heating-cooling-heating) and its compensated signal. **c** Change in the measured voltage of the GSR and measurement of the temperature against sweat generation. **d** Change in the measured voltage of the GSR sensor and measurement of the temperature under the different anatomical locations.

coverage of a sedentary subject, as shown in Fig. 3a. The devices mounted at the locations of interest yield real-time readings of pressure, temperature, and hydration in a fast (~ 10 Hz), sequential readout scheme based on NFC protocols from four primary antennas integrated with a multiplexer and an NFC reader located below the seat of the wheelchair, as depicted in Fig. 3b. Supplementary Fig. 15 shows the two portable batteries connected to the multiplexer and the NFC reader power the system to work for more than 16 h, allowing continuous measurement of pressure, temperature, and hydration for several days by recharging the batteries. The wood frames and their partitions support stable operation of the system with full coverage regardless of whether the wheelchair is stationary or in motion. The soft foam mattress adopted with the wood frames to minimize the generation of device-related pressure injuries with skin irritation. The high softness of the soft foam mattress reduces the pressure concentration on the sensor at the skin-mattress interfaces. (Supplementary Fig. 16) Visualization of data and control of the integrated system are possible through portable electronic devices (e.g., Tablet PC, Smartphone) via the mobile communication. (Supplementary Movie 1) Fig. 3c(i-iv) presents the simulation results for the magnetic field distribution, direction, and strength of the four multiplexed antennas in XYZ coordinates. The four multiplexed antennas with different sizes ($32\text{ cm} \times 34\text{ cm} \times 3\text{ cm}$ for antennas 1 and 2; $20\text{ cm} \times 16\text{ cm} \times 3\text{ cm}$ for antennas 3 and 4) support sufficient magnetic field strength over the required operating distance with negligible electromagnetic interference. Figure 3d shows the experimental measurements for the operating range of the wireless sensor from each antenna that supports a maximum distance of more than 10 cm perpendicular to each primary coil to cover the entire area of the wheelchair in a sequential mode. The multiplexed antennas 1, 2, 3, and 4 can operate over maximum distances of 32, 24, 32 and

32 cm along the central axis of each primary antenna, respectively. These results indicate that the four multiplexed antennas provide stable power delivery and data communication with the sensors mounted at multiple locations on a subject sitting in a wheelchair. In addition, they support capabilities for continuous monitoring of pressure, temperature, and hydration of the movable sensing system under postural changes of the subject while stationary or in motion. Supplementary Fig. 17a shows the measurement results of operating range obtained at the centers of four multiplexed antennas, that the device can no longer communicate via NFC. The multiplexed antenna can operate over maximum distances of 38.5, 42, and 36 cm in the Z direction at an operating power of 12 W. Supplementary Fig. 17b shows the wireless sensing characteristics of the pressure sensor at different positions at $z = 10\text{ cm}$ height above primary antenna 2. The average output of the pressure sensor is $25.6\text{ mV} @ 50\text{ kPa}$ with a low standard deviation. ($\sigma = 0.47\text{ mV}$) These results indicate that the device shows stable wireless signals with a low fluctuation of ADC under wireless communication.

Sensing performance and stability evaluation of the battery-free, wireless sensor

The sensor platform design and sequential RF readout scheme facilitate simultaneous measurement of pressure, temperature, and hydration at multiple locations in a wireless, battery-free mode. Figure 4a presents the responses of the wireless pressure sensor to loading and unloading between 0 kPa and 100 kPa. These results exhibit a linear response ($R^2 = 0.982$) with minimal hysteresis ($< 0.1\%$). Supplementary Fig. 18a depicts the stability of the device under 100 cyclic loadings of 70 kPa. Supplementary Fig. 18b, c shows the responses of the wireless pressure sensors with different metal film types under the different pressures. Owing to the high

sensitivity of the nano-cracked metal film, the crack-activated pressure sensor shows high signal to noise ratio (SNR = 417.4) under the 100 kPa compared to the sensor with no cracks (SNR = 127.32). Figure 4b shows the change in the measured voltage for the wireless pressure sensor based on the temperature variation (heating-cooling-heating). The change in the measured voltage from the wireless pressure sensor is consistent with the temperature change measured using the temperature sensor (NTC). These results enable the removal of the temperature effect from the pressure sensor response using the compensation equation. (Supplementary Fig. 19) In addition, sensing performance and stability evaluation of the device in the system is essential in both the moving and stationary states. Supplementary Fig. 20a presents the change in the measured voltage from the pressure and temperature sensors while moving with a speed of 1.1 km h^{-1} on a flat asphalt road. These results mean that the wireless pressure sensor yields a high signal-to-noise ratio (SNR = 82.1) under a pressure of 70 kPa loading with negligible drift ($<0.2\%$), even during motion. The SNR was calculated using the following Eq. 1⁵⁸:

$$\text{SNR} = \Delta V_{\text{average}} / \sigma_{\text{baseline}} \quad (1)$$

where $\Delta V_{\text{average}}$ is the average change in the measured voltage, and σ_{baseline} is the standard deviation of the baseline. Supplementary Fig. 20b shows the changes in the measured voltage from the pressure and temperature sensors while moving from indoors (21.8°C) to outdoors (23.6°C). These results indicate that the temperature dependence of the responses of the wireless pressure sensor can be compensated using the change in the measured voltage obtained from the NTC regardless of the ambient temperature variation. Supplementary Fig. 20c shows the change in the measured voltage from the wireless pressure sensor while moving at two different speeds. These findings demonstrate the stability of the signal at different speeds ranging from 1.1 km h^{-1} to 3.3 km h^{-1} when in motion independently or with the help of a caregiver. Supplementary Fig. 20d shows the change in the measured voltage from the pressure sensor and NTC while an elevator ascends and descends. These results reveal that the signal is stable and does not exhibit discontinuous periods when the velocity and acceleration of the system vary inside the elevator. Supplementary Fig. 20e presents the changes in the measured voltage in the absence of loading when the system is moving on an inclined surface ($+7^\circ$) and a declined surface (-7°). These results indicate that the output signals obtained from the pressure and temperature sensors are stable signals with negligible drifts (0.25%) regardless of the ground slope. Supplementary Fig. 20f compares the changes in the measured voltage when the system is moving on four different ground surfaces, including asphalt, urethane, polyethylene and grass. The noise levels at these ground surfaces are 0.5% , 0.2% , 0.5% , and 0.7% , which are negligible compared to the changes in the measured voltage under the loading, as shown in Supplementary Fig. 20a. Figure 4c compares responses of temperature and GSR sensors mounted at the spinous process before and after sweating. The change in measured voltage (ΔV_{sweat}) of the GSR sensor significantly increased with sweating while keeping the response of temperature constant at 34.5°C . Figure 4d presents the responses of the GSR sensor mounted at locations of interest prone to developing the pressure injuries before and after sweating. These results indicate that all mounting locations of device increases ΔV_{sweat} of GSR sensor, which can be calibrated using a fitting equation for skin hydration level, as shown in Supplementary Fig. 14b.

Continuous measurement of pressure, temperature, and hydration with a human subject

Validation trials for a human subject in a wheelchair while in motion and stationary are important for the extension of this sensor system

to clinical studies. In this study, these evaluations included continuous measurement of pressure, temperature, and hydration at multiple locations of a healthy subject (male, 30-year-old; mass, 71 kg; height, 180 cm; skin temperature $\sim 36^\circ\text{C}$) sitting in a wheelchair while in motion in both indoor and outdoor environments.

The trials in this study involved continuous measurement of pressure, temperature, and hydration at multiple locations with changes in posture of the subject sitting in a wheelchair for pressure relief. Figure 5a shows the mounting locations of devices that are known to be susceptible to pressure injuries in the sitting position, including on the heels (1 and 2), posterior thighs (3 and 4), sacrum (5 and 6), and spinous processes of upper, mid, and lower back (7 and 9), as shown in Supplementary Fig. 21. Figure 5b depicts infrared (IR) photographs of the subject that show distinct changes in the sitting posture at different times. These changes in posture depend on various weight shifts, suggested by NPIAP, including (ii) a push-up weight shift, (iii, iv) a lateral weight shift, (v) an anterior weight shift, and (vi) lifting both feet. The subject kept each pose for 1 min after weight shifts, and then kept it for 3 min after returning to the original posture (i), which is a base position. Figure 5c presents the results of continuous measurement of pressure, temperature, and hydration obtained from each of the mounting locations under posture changes in the sitting position. In particular, the collected data from the multiple sensors provide not only the pressure relief and its range on one location of interest, but also an increase or a decrease in pressure on another mounting locations at the same time under postural change. As expected, the data collected during the push-up weight shift in Fig. 5b(ii) exhibit pressure relief at the posterior thighs, tailbone, and scapulae with increasing pressure at both heels. The data obtained during the lifting of two feet in Fig. 5b(vi) show the pressure relief at the two heels with increasing pressure at the posterior thighs and tailbone. These results show relatively high pressures (average pressure of 18.6 kPa and 22.7 kPa, respectively) and their changes (i.e., difference between maximum and minimum pressures; 14.3 kPa and 25 kPa) on mounting locations of sensors 5 and 6. Although the pressure and its change depend on a weight, a muscle strength, and degree of paralysis for each body part under postural change, the results can provide a quantitative basis for yielding medical information of body parts using the developed technology. The maximum values of pressure are 17.1 kPa at heel in the anterior weight shift, 9.43 kPa at posterior thigh by the anterior weight shift, 37.5 kPa at tailbone by lifting both feet, respectively. The measured values of pressure at spinous processes are below 10 kPa. These results provide a quantitative basis to determine the pressure, duration and level of physical activity at mounting locations of the device under changes in a sitting posture. The skin temperatures are in the range of 22.0 – 34.1°C , which are in good agreement with those observed by the IR camera (21.4 – 35.0°C). In particular, the skin temperature is kept constant in all mounting locations with relatively low values ($<25^\circ\text{C}$) on mounting locations of sensors 1 and 2. The skin hydration level is in the range of 49.2 – 85.4% at mounting locations of device under various weight shifts. In particular, the skin hydration levels measured on mounting locations of sensors 3–6 are relatively high ($>80\%$).

Continuous measurement of pressure, temperature and hydration in SCI patients

The clinical studies conducted in this study involved two SCI patients with a high risk for developing the pressure injuries caused by sitting. One patient was a 56-year-old male, hospitalized SCI patient with a cervical fracture at the C4 level, with a height of 167 cm, a weight of 65 kg, blood pressure of 120/80 mmHg, albumin of 4.3 g/dl, and hemoglobin A1c (HbA1c) of 6.2%. Figure 6a(i) provides a photograph of the SCI patient moving in the wheelchair with the help of a caregiver in the hospital. The red

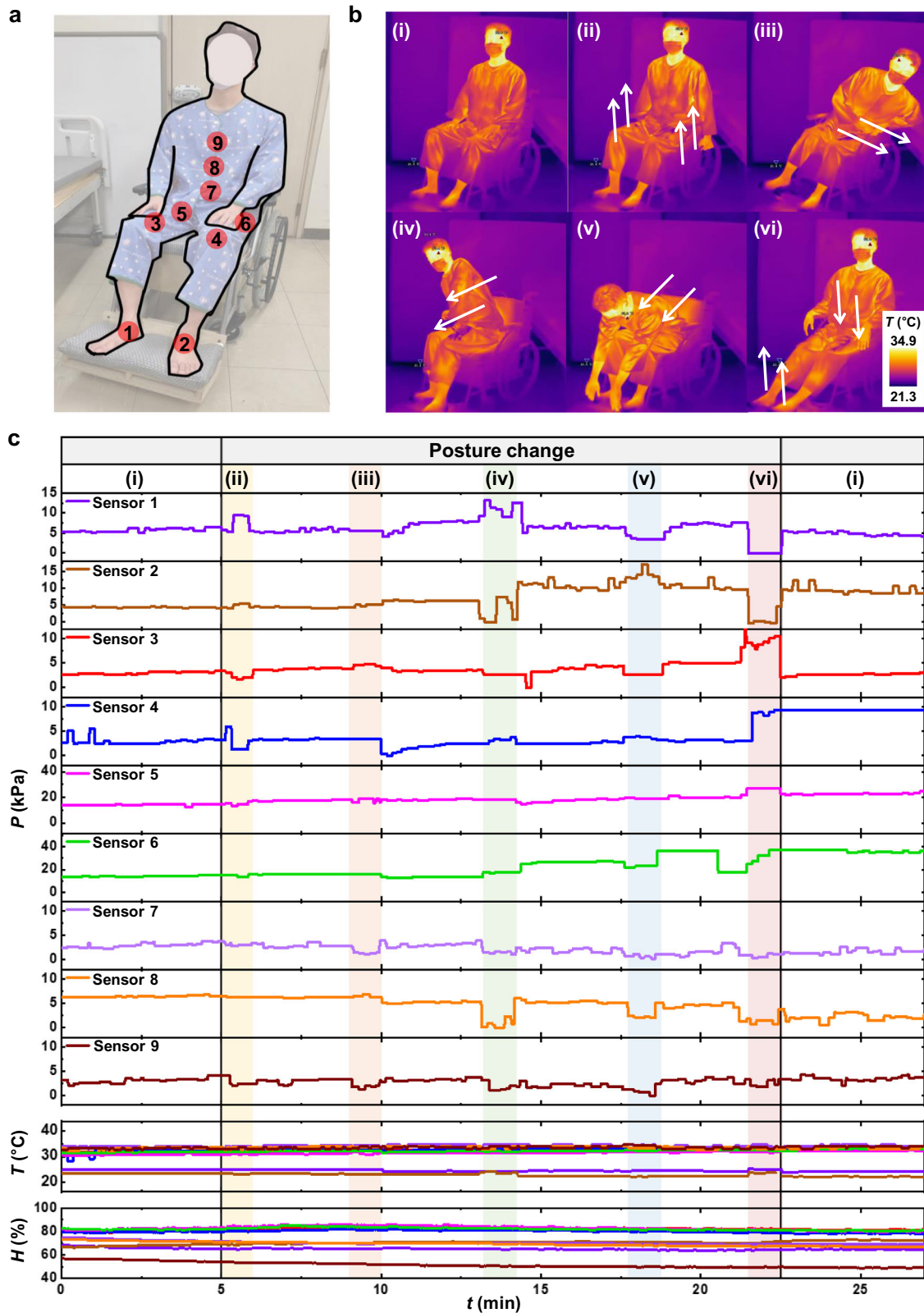


Fig. 5 Continuous measurement of pressure, temperature, and hydration from a healthy subject. **a** Photograph of the subject sitting in a wheelchair. Red discs mark the mounting locations of the devices. **b** IR images of postural changes of the subject for self-repositioning. (i) Base position. (ii) Push-up weight shift. (iii) Left-side lateral weight shift. (iv) Right-side lateral weight shift. (v) Anterior weight shift. (vi) Lifting both feet. **c** Results from continuous measurement of pressure, temperature, and hydration from each of the sensors under posture changes in the sitting position. The subject agreed with the distribution of these photographs using a content form in Supplementary Fig. 24.

disks indicate the locations of eight devices mounted at the heels (1 and 2), posterior thighs (3 and 4), sacrum (5), and spinous processes in the upper, mid, and lower back (6, 7, and 8). Figure 6a(ii–iv) shows photographs of the SCI patient engaging in changes in sitting posture for pressure relief (weight shift, 1 min) by himself while stationary. Figure 6b presents the results of continuous measurement of pressure, temperature, and hydration obtained from each of the mounting locations. The collected data shows relatively large pressures (average pressure of 30.1 kPa, 33.2 kPa, and 39.5 kPa) and their changes (9.4 kPa, 12.1 kPa, and 5.13 kPa) on mounting locations of sensors 3–5 in spite of the patient with a light weight of 65 kg compared to the healthy subject (71 kg). The data measured during the right weight shift in Fig. 6a(ii) reveals pressure relief at the left posterior thigh and left back with increasing pressure in the right posterior thigh. In addition, the data collected during the anterior weight shift in Fig. 6a(iv) exhibit an increase in pressure in plots 1–5 with decreasing pressure in plots 6–8. The maximum value of pressure is 42.5 kPa at the sacrum in the anterior weight shift. As expected, the anterior weight shift should be avoided for prevention of pressure injuries due to a significant increase in the pressure on these locations. While moving in wheelchair inside a hospital (very low roughness of ground surface), changes in pressure on mounting locations occurs due to spontaneous weight shifts. However, these changes in pressure are very small compared to those caused by the weight shifts for the pressure relief. In particular, the average pressures on mounting locations of sensors 3–5 are 30.3 kPa, 36.4 kPa, and 39.3 kPa with their changes of 0.6 kPa, 3.83 kPa, and 1.82 kPa while moving, respectively. These results indicate a relatively high risk for developing the pressure injuries caused by sitting without proper weight shifts for the pressure relief. The skin temperature and hydration level of the SCI patient are in the range of 24.0–33.4 °C and 49.2–83.7%, respectively. The skin temperatures are in the range of 31.9–32.9 °C on the mounting locations of sensors 3–5 while the skin hydration levels increased. These results indicate that the skin temperature does not significantly depend on the change in skin hydration level caused by the sweat generation and evaporation.

The other SCI patient was a 63-year-old male with a cervical fracture at the C4 level who regularly visited hospital for outpatient treatment (Fig. 7). This patient had a height of 170 cm, a weight of 70 kg, blood pressure of 130/90 mmHg, albumin of 5.1 g/dl, and HbA1c of 6.3%. Figure 7a(i) indicates the five mounting locations (red disks), including the heels (1 and 2), posterior thighs (3 and 4), and spinous processes in the upper back (5). Figure 7a(i–iii, v) shows photographs of the SCI patient moving in the wheelchair with caregivers at different times during the feasibility test, including (i–iii) outdoors over uneven surfaces and (v) indoors on smooth surface. Figure 7a(iv) presents a photograph of the patient engaging in an anterior weight shift for pressure relief by himself while waiting to see a doctor for rehabilitation treatment in hospital. Figure 7b shows the results of continuous measurement of pressure, temperature, and hydration from each mounting location while moving or stationary in the wheelchair indoors and outdoors. The collected data exhibit stable, continuous signals regardless of the condition of the ground surface condition and surrounding temperature (indoor: 23.8 °C, outdoor: 25.5 °C). The skin temperature of the SCI patient is in the range of 25.0–32.8 °C. Interestingly, the SCI patient moving in the wheelchair on uneven surfaces (outdoor) shows an increased activity in the paralyzed parts, as shown in plots 1 and 2, compared to those presented in plots 3–5. The collected data shows relatively large pressures (average pressure of 23.4 kPa, 23.5 kPa, and 18.2 kPa) and their changes (2.7 kPa, 1.6 kPa, and 2.9 kPa) on the mounting locations of sensors 3–5. As expected, the data obtained during the anterior weight shift in Fig. 7b(iv) exhibit a decrease in pressure at the back (5) with increasing pressure on both sides of the heels (1 and 2) and posterior thighs (3 and 4).

The maximum value of pressure is 24.8 kPa at the posterior thigh (right-side) in the anterior weight shift. While moving in wheelchair outdoor, changes in pressure on the mounting locations occurred due to spontaneous weight shifts and a relatively high roughness of ground surfaces. However, these changes in pressure while moving outdoor was very small compared to those caused by the anterior weight shifts for the pressure relief. These results indicate that the system provides a quantitative basis to determine not only the pressure and duration, but also the level of actual activity of the paralyzed parts while stationary or moving in the wheelchair indoors and outdoors. In addition, the skin temperatures were in the range of 30.8–32.8 °C on the mounting locations of sensors 3–5 regardless of changes in the skin hydration level. The skin hydration levels on the mounting locations of sensors 3 and 4 gradually increased from 57.7 to 76.1% and from 58.6% to 80.8%, respectively, due to sweat generation. On the other hand, the skin hydration level on the mounting location of sensor 5 showed relatively high value of 75.1%. These data indicate that the mounting locations of sensors 3–5 could be at higher risk for developing the pressure injuries due to the combination of the prolonged high pressure and hydration level. Supplementary Fig. 22 presents the statistical analysis about the ulcer-related variables of the subjects that were measured in Figs. 5–7. As shown in Supplementary Fig. 22a, the measured pressure of the wheelchair patient is concentrated on the lower body (e.g., high, sacrum), especially in the case of hospitalized patients. The changes of the pressure according to the postural change in clinical trials are more pronounced in healthy patients compared to paraplegic patients. (Supplementary Fig. 22d) Supplementary Fig. 22b shows the average and deviation of the measured temperatures of the subject 1–3, and its deviation between patients was smaller than those of pressure and hydration. The heel, the undressed area of the patients, shows the lowest temperature for all the patients. (Supplementary Fig. 22e) Supplementary Fig. 22c and Supplementary Fig. 22f show the hydration level of the pressure injury risk area of subject 1–3. Hospitalized patients show slightly lower measured value of the hydration than a healthy subject. (Supplementary Fig. 22f).

DISCUSSION

This paper introduced a battery-free, wireless, multimodal sensors and movable sensing system that supports continuous monitoring of pressure, temperature, and hydration from multiple devices located at the skin interfaces of a subject who is moving or stationary in a wheelchair. The resulting data collected from pressure, temperature, and GSR sensors at multiple critical locations provides an accurate, and quantitative means of preventing the pressure injuries caused by sitting in wheelchair users. The nanoscale encapsulation of cracked metal films supports a reliable pressure sensor that shows high sensitivity as well as low hysteresis, high linearity and long-term stability over a wide range of pressures (~100 kPa). In addition, the movable sensing system with battery-free, wireless sensing platforms provides stable and long-range communication capabilities for multiple mounting locations of interest while the wheelchair moves forward, backward, up and down. Experimental and numerical simulation results obtained for the device, and the results of clinical trials on SCI patients demonstrated the feasibility and stability of the battery-free, wireless sensor and movable sensing system. In particular, the high sensitivity and low hysteresis of the sensor, as well as the stability of the system on various ground surfaces, enabled continuous monitoring of pressure, temperature, and hydration while moving and stationary in the wheelchair. As a pioneer approach, these results offer advanced route to develop the sensor and system for prevention of pressure injuries caused by sitting. Supplementary Tables 1–2 summarizes the detailed information about the developed

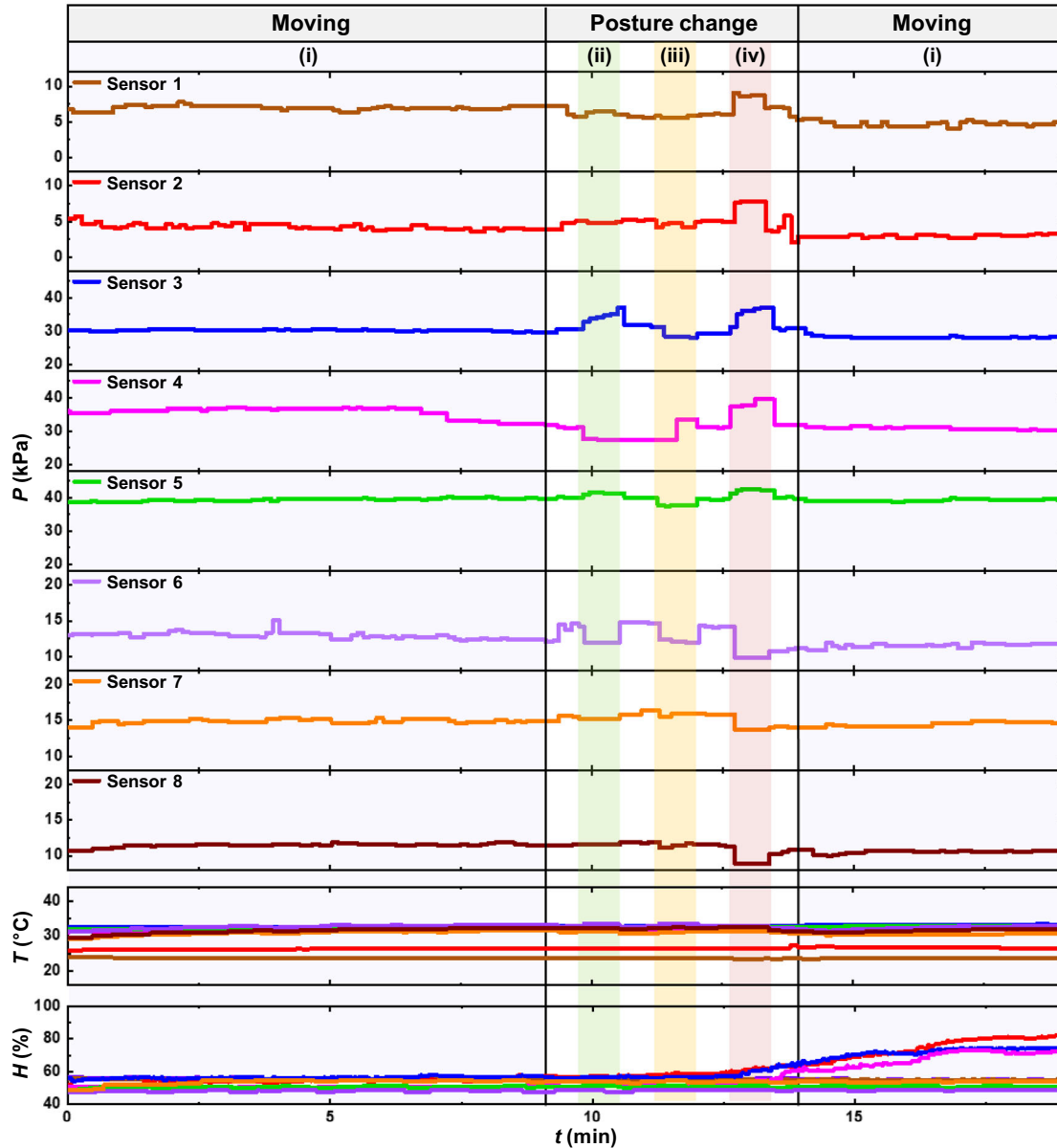
a**b**

Fig. 6 Continuous measurement of pressure, temperature, and hydration from a hospitalized, paraplegic patient with spinal cord injury. **a** Photographs of wheelchair moving and postural changes of the subject for self-repositioning. (i) Indoor moving with the caregiver in the hospital. Red discs mark the mounting locations of the devices. (ii) Right-side lateral weight shift. (iii) Left-side lateral weight shift. (iv) Anterior weight shift. **b** Results from continuous measurements of pressure, temperature, and hydration from each of the sensors while moving or stationary weight-shift in the wheelchair. The subject agreed with the distribution of these photographs using a content form in Supplementary Fig. 25.

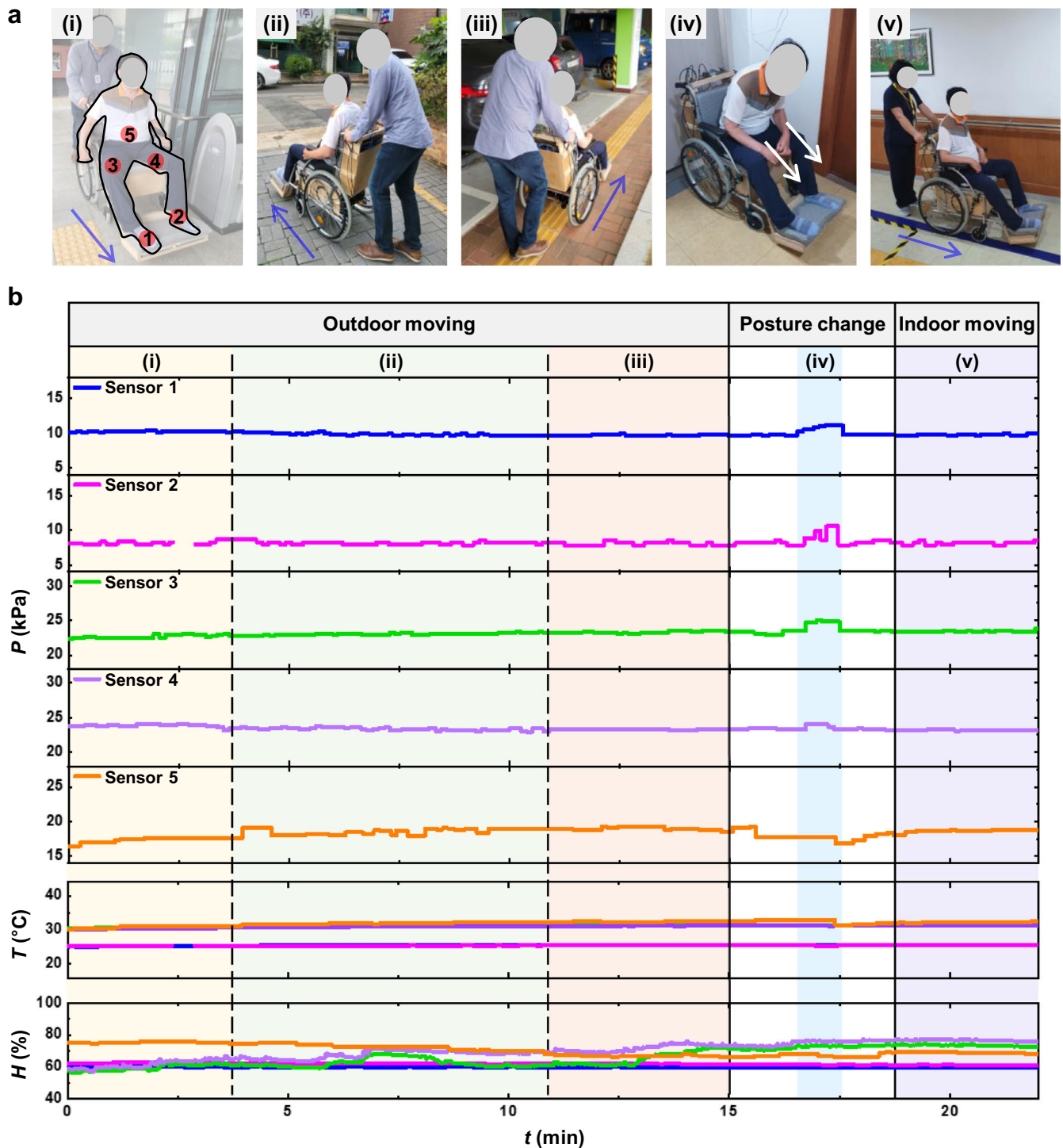


Fig. 7 Continuous measurement of pressure, temperature, and hydration from a paraplegic patient with spinal cord injury that regularly came to the hospital for outpatient treatment. **a** Photographs of wheelchair moving and postural changes of the subject for self-repositioning. (i) Outdoor moving with the caregiver. Red discs mark the mounting locations of the devices. (ii) Outdoor moving over uneven sidewalk. (iii) Outdoor moving over smooth sidewalk. (iv) Anterior weight shift. (v) Indoor moving in the hospital. **b** Results from continuous measurements of pressure, temperature, and hydration from each of the sensors while moving or stationary weight-shift in the wheelchair. The subject agreed with the distribution of these photographs using a content form in Supplementary Fig. 26.

pressure sensor system in the aspects of sensor specification, design of the system, and clinical trials, compared to the previously reported platforms^{25–28}.

This movable sensor system could help to prevent the pressure injuries caused by sitting for SCI patients, and for patients in a

wheelchair who have acute activity reduction in specific areas due to accidents or surgery. In addition, the data collected from an increased number of sensors strategically deployed at locations of interest provides medical information regarding the spatiotemporal pressure, temperature, and hydration distributions at critical skin

interfaces of these patients. The additional sensors, including those measuring shear force or skin erythema in the battery-free, wireless sensing platforms could enhance our understanding of the mechanism by which the skin is damaged. Finally, clinical studies conducted on numerous patients using the sensors and system reported herein will support the definition of correlations, algorithms, and quantitative thresholds for the risk of developing the pressure injuries caused by sitting, which is useful for precision healthcare of the patients along with machine learning analysis.

METHODS

Fabrication of the battery-free, wireless sensing platform

Fabrication began by mounting the electronic components for the designed circuit on a flexible PCB substrate (Pyrulux AP8535R, DuPont). The electronic components included an NFC SoC (RF430FRL152H, Texas Instruments), an instrumentation amplifier (INA333, Texas Instruments), resistors (RC0603 FR-07, Yageo), and capacitors (Samsung Electro-Mechanics), which were electrically connected using solder paste (SMDLTLFP10T5, ChipQuik) and a solder wire (SACX0307, Alpha Metal). The overall size of sensing platform is $35 \times 56 \text{ mm}^2$, including the round coil antenna of flexible PCB ($d = 30 \text{ mm}$), serpentine interconnector ($9 \times 6 \text{ mm}^2$), and pressure, temperature, hydration sensor. ($8 \times 8 \times 2 \text{ mm}^3$) The NFC SoC converted the analog signal to a digital signal for wireless communication through the internal 3 ADCs with a 14-bit resolution, and transmitted the data to the wireless reader by NFC. The resonant frequency for wireless communication was adjusted by low-loss tuning capacitors (GJM03-KIT-TTOL-DE, Murata Electronics) according to the inductance value of the designed RF loop antenna for implementation with high-quality factors at the resonant frequency. A Wheatstone bridge circuit, connected to the pressure sensor, converts a change in the resistance of the pressure sensor into a change in voltage, which was passed to the instrumentation amplifier and delivered to one pin connected with internal ADC in the NFC SoC. A voltage divider, connected to the NTC thermistor (NTCG064EF104FTBX, TDK Corporation), converts a change in the resistance of the NTC into a change in voltage, which was delivered to another pin connected with internal ADC in the NFC SoC. In addition, a voltage divider, connected to two metal pads as a GSR sensor, converts a change in the conductivity of skin into a change in voltage, which was delivered to the other pin connected with internal ADC in the NFC SoC. The values of the pressure, temperature, and hydration sensors were converted to digital data for wireless communication using an internal ADC alternately, and the operation of the internal ADC was controlled by the embedded code of the NFC SoC. In addition, every component of the wireless platform operated with the power delivered from an NFC reader through the NFC SoC.

Fabrication of crack-activated metal film with nanoscale encapsulation

The process began by spin coating a PI solution (1000 rpm for 60 s) onto a Si wafer, followed by curing the PI solution in the convection oven (150°C for 30 min and 250°C for 4 h). A PI film with a thickness of $75 \mu\text{m}$ was formed on the Si wafer after four repeated processes of spin coating and curing. Photolithography defined a resist pattern (AZ nLOF 2035, MicroChem) on the PI film to enable patterning of a bilayer of Cr/Au ($10 \text{ nm}/30 \text{ nm}$ in thickness) deposited by electron beam evaporation *via* a liftoff process. The Cr/Au patterns on the PI film after the delamination wafer were repeatedly stretched to a strain of 4% at a rate of $1 \text{ mm}/\text{min}$ by 100 times using a customized linear stage to generate cracks on the patterned Cr/Au film. Polyethylene-C ($80\text{--}200 \text{ nm}$ in thickness) was coated on top of the cracked metal layers to yield an encapsulation layer *via* chemical vapor deposition (NRPC-500, Nuritech). Mesh contact pads was formed by RIE

(O_2 , 100 mTorr , 100 W , 20 sccm , 20 min) and the free-standing film was cut with two opening cuts ($2 \times 0.25 \text{ mm}^2$) to define the outline with a direct UV (355 nm) laser ablation system (ProtoLaser U4, LPKF) resulting in the formation of the tri-layered film.

Assembly of the pressure sensor

A glass wafer was prepared using a UV laser system (ProtoLaser U4, LPKF). Next, electron beam evaporation of Cr/Au ($20 \text{ nm}/100 \text{ nm}$ in thickness) through a shadow mask yielded patterns of electrical traces on the glass substrate as a rigid substrate, followed by bonding a piece of a cover glass ($3 \times 4 \times 0.15 \text{ mm}^3$) using an epoxy resin (Loctite Epoxy Instant Mix 5 min, Loctite). The cover glass as a rigid sheet included an opening cut ($2 \times 2 \text{ mm}^2$) in the center to enable both alignment and deflection of the tri-layered film and two opening cuts ($0.7 \times 0.7 \text{ mm}^2$) for electrical connection using a UV laser system (ProtoLaser U4, LPKF). A tri-layer film (PI/Au/PI film with thicknesses of $75/0.03/10 \mu\text{m}$; $3 \times 4 \times 0.075 \text{ mm}^3$) with lithographically defined patterns of Au and two opening cuts ($2 \times 0.25 \text{ mm}^2$) was bonded to the top surface of the rigid sheet, with electrical connections to the Cr/Au patterns on the rigid substrate formed using Ag epoxy (8331-14G, MG chemicals). A soft pad of PDMS ($1.5 \times 1.5 \times 0.265 \text{ mm}^3$) was mounted on a suspended region between the opening cuts on the tri-layer film without chemical bonding to ensure conformal contact and stable operation under loading/unloading cycles. The rigid frame (Si, $7 \times 7 \text{ mm}^2$ inner lateral dimensions, $8 \times 8 \text{ mm}^2$ outer lateral dimensions, and 0.5 mm thickness) was mechanically bound using epoxy resin on the edge of the glass substrate. The membrane film (polyimide, $8 \times 8 \times 0.075 \text{ mm}^3$) and a rigid square pad (Si, $3 \times 3 \times 0.5 \text{ mm}^3$) was bonded on the center of the film to deliver the vertical load to the tri-layered film. The soft frame (Dragonskin10, $6 \times 6 \text{ mm}^2$ inner lateral dimensions, $8 \times 8 \text{ mm}^2$ outer lateral dimensions and 0.5 mm thickness) was bonded on the membrane film. Further, treatment of the soft frame with (3-mercaptopropyl) trimethoxysilane (MPTMS, 95%, Sigma-Aldrich) increased the bonding strength on the PI film using an epoxy resin⁵⁹. Finally, a rigid cover layer (Si, $8 \times 8 \times 0.5 \text{ mm}^3$) was placed on the soft frame and the rigid pad to form a physical interface.

NFC protocol and operation of the movable sensing system

A wireless reader (TRF7970AEVM, Texas Instruments), connected to a notebook, was used to control the writing process in an NFC SoC using a custom graphical user interface according to ISO 15693. The NFC SoC provided data communication and wireless energy harvesting by the antenna reader (ID ISC. LRM2500-A, FEIG) with a transmission antenna. ISOStart 2018 software supported continuous, real-time data acquisition of ADC values from the NFC SoC. Application software, developed using Python, enabled the classification and visualization of the collected data. Supplementary Fig. 23 shows the reading procedure of NFC protocol software (ISOStart 2018.Feig electronic) for data acquisition of 9 sensors with four multiplexed antennas during the experiment in Fig. 5 (antenna 1, behind the backrest; antenna 2, below the seat; and antennas 3 and 4, below the footrest). NFC protocol software switches each of the antennas for 1600 ms , followed by the ADC output values of the pre-identified sensors per 50 ms . The wheelchair included several wood partitions to protect the four antennas, the wireless reader and the four-channel multiplexer (ID ISC.ANTMUX.M4, FEIG electronic), and two portable batteries (NEXT-408PB-UPS, Next Network) from external forces. The four multiplexed antennas integrated with the wheelchair consisted of two HF loop antennas (ID ISC.ANT 310/310, FEIG electronic) for coverage of the back and hip areas and two HF handheld antennas (ID ISC.ANT200/200, FEIG electronic) for coverage of the footrest area, respectively. In addition, the wireless reader and four-channel multiplexer (ID ISC.ANTMUX.M4, FEIG electronic,

Supplementary table 3) were connected to two portable batteries for power supply.

Sensor characterization

The pressure sensor was tested using a high-precision universal testing machine (AG-X plus, Shimadzu) to measure the normal pressure and a digital multimeter (NI-USB 4065 Digital Multimeter) to measure the resistance of the sensor. In addition, a microactuator (MA-35, Physik Instruments) and force transducer (SM-500N, Interface) were used to measure the cyclic response of the sensor.

Electromagnetic simulation of the multiplexed antenna systems

The commercial software ANSYS HFSS was used to determine the magnetic field around the rectangular reader antennas on the wheelchair at 13.56 MHz. Copper wire with a radius of 2.5 mm was used to model the antennas using the default material properties for copper included in the HFSS library. A cubic radiation boundary (side of 2000 mm) and tetrahedral elements with adaptive mesh convergence were used to ensure computational accuracy. Lumped ports were used to turn individual antennas on or off and calculate the magnetic field.

Finite element analysis

The commercial software ABAQUS was used to evaluate the deformation of the interconnect Cu layer within the elastic region under mechanical deformations of stretching and bending. The PDMS packaging (400 μm in thickness), Cu (18 μm in thickness), and PI (75 μm in thickness) layers were modeled using the S5R element, which was a 3D, doubly-curved, four-node shell element. The size of the element was determined at the level of ensuring convergence and accurate results. The mechanical properties of the material used for the analysis were $E_{\text{PI}} = 2.5 \text{ GPa}$ and $\nu_{\text{PI}} = 0.34$ for PI; $E_{\text{Cu}} = 110 \text{ GPa}$, $\nu_{\text{Cu}} = 0.36$ for Copper; $E_{\text{PDMS}} = 1 \text{ MPa}$, $\nu_{\text{PDMS}} = 0.49$ for PDMS. In addition, ABAQUS was used to evaluate stress concentration and relaxation in the region of cracked metal under bending stress. The cracked metal and encapsulation were modeled using CPS5R elements with 2D structural analysis. The mechanical properties of the material used for the analysis were $E_{\text{Au}} = 79 \text{ GPa}$ and $\nu_{\text{Au}} = 0.42$ for Au; $E_{\text{PC}} = 4.5 \text{ GPa}$, $\nu_{\text{PC}} = 0.4$ for Polyethylene-C.

Clinical trial protocol with hospitalized patients

This clinical trial was approved by Institutional Review Board of Pusan National University Hospital (2111 017 109). The clinical trial was registered on the Clinical Research Information Service (CRIS) Republic of Korea. (Registration number: KCT0007094, Registration date: 2022.03.18) After understanding the contents of the study and signing consent forms in Supplementary Figs. 17–19, volunteers recruited from the population of the study site (Kimhae Hansol Rehabilitation & Convalescent Hospital) participated in the clinical trial. The volunteers include healthy subjects and patients with SCI, while those with pressure injuries were excluded from the trials by considering the medical records of the volunteers, including age, sex, height, weight, paralysis, serum albumin level, and HbA1c level. After the clinical trials, doctors visually checked the skin condition of patients at each mounting location to identify any skin abnormalities.

DATA AVAILABILITY

Additional data related to this paper may be requested from the corresponding authors upon reasonable request.

Received: 16 September 2022; Accepted: 11 January 2023;
Published online: 10 February 2023

REFERENCES

- Schwartz, D., Magen, Y. K., Levy, A. & Gefen, A. Effects of humidity on skin friction against medical textiles as related to prevention of pressure injuries. *Int. Wound J.* **15**, 866–874 (2018).
- Zeevi, T., Levy, A., Brauner, N. & Gefen, A. Effects of ambient conditions on the risk of pressure injuries in bedridden patients—multi-physics modelling of micro-climate. *Int. Wound J.* **15**, 402–416 (2018).
- Kovindha, A., Kammuang-Lue, P., Prakongsai, P. & Wongphan, T. Prevalence of pressure ulcers in Thai wheelchair users with chronic spinal cord injuries. *Spinal Cord.* **53**, 767–771 (2015).
- Li, Z., Lin, F., Thalib, L. & Chaboyer, W. Global prevalence and incidence of pressure injuries in hospitalised adult patients: A systematic review and meta-analysis. *Int. J. Nurs. Stud.* **105**, 103546 (2020).
- European Pressure Ulcer Advisory Panel and National Pressure Ulcer Advisory Panel, P. P. P. I. A. *Prevention and Treatment of Pressure Ulcers: Quick Reference Guide. Clinical Practice Guideline* (2014).
- Carrigan, W. et al. Design and operation verification of an automated pressure mapping and modulating seat cushion for pressure ulcer prevention. *Med. Eng. Phys.* **69**, 17–27 (2019).
- Gutierrez, E. M., Alm, M., Hultling, C. & Saraste, H. Measuring seating pressure, area, and asymmetry in persons with spinal cord injury. *Eur. Spine J.* **13**, 374–379 (2004).
- Hubli, M. et al. Feedback improves compliance of pressure relief activities in wheelchair users with spinal cord injury. *Spinal Cord.* **59**, 175–184 (2021).
- Gefen, A. The biomechanics of sitting-acquired pressure ulcers in patients with spinal cord injury or lesions. *Int. Wound J.* **4**, 222–231 (2007).
- Thorfinn, J., Sjöberg, F. & Lidman, D. Sitting pressure and perfusion of buttock skin in paraplegic and tetraplegic patients, and in healthy subjects: A comparative study. *Scand. J. Plast. Reconstr. Surg. Hand Surg.* **36**, 279–283 (2002).
- Byrne, D. W. & Salzberg, C. A. Major risk factors for pressure ulcers in the spinal cord disabled: A literature review. *Spinal Cord.* **34**, 255–263 (1996).
- Shiferaw, W. S., Akalu, T. Y., Mulugeta, H. & Aynalem, Y. A. The global burden of pressure ulcers among patients with spinal cord injury: A systematic review and meta-Analysis. *BMC Musculoskelet. Disord.* **21**, 334 (2020).
- Brem, H. et al. High cost of stage IV pressure ulcers. *Am. J. Surg.* **200**, 473–477 (2010).
- Allman, R. M., Goode, P. S., Burst, N., Bartolucci, A. A. & Thomas, D. R. Pressure ulcers, hospital complications, and disease severity: impact on hospital costs and length of stay. *Adv. Wound Care* **12**, 22–30 (1999).
- Smith, S., Snyder, A., McMahon, L. F. J., Petersen, L. & Meddings, J. Success In hospital-acquired pressure ulcer prevention: a tale in two data sets. *Health Aff.* **37**, 1787–1796 (2018).
- Graves, N., Birrell, F. & Whitby, M. Effect of pressure ulcers on length of hospital stay. *Infect. Control Hosp. Epidemiol.* **26**, 293–297 (2005).
- Kottner, J. et al. Prevention and treatment of pressure ulcers/injuries: The protocol for the second update of the international Clinical Practice Guideline 2019. *J. Tissue Viability* **28**, 51–58 (2019).
- Stephens, M. & Bartley, C. A. Understanding the association between pressure ulcers and sitting in adults what does it mean for me and my carers? Seating guidelines for people, carers and health & social care professionals. *J. Tissue Viability* **27**, 59–73 (2018).
- Sharp, C. A., Schulz Moore, J. S. & McLaws, M.-L. Two-hourly repositioning for prevention of pressure ulcers in the elderly: patient safety or elder abuse? *J. Bioeth. Inq.* **16**, 17–34 (2019).
- Sae-Sia, W., Wipke-Tevis, D. D. & Williams, D. A. The effect of clinically relevant pressure duration on sacral skin blood flow and temperature in patients after acute spinal cord injury. *Arch. Phys. Med. Rehabil.* **88**, 1673–1680 (2007).
- Sae-Sia, W., Wipke-Tevis, D. D. & Williams, D. A. Elevated sacral skin temperature (Ts): A risk factor for pressure ulcer development in hospitalized neurologically impaired Thai patients. *Appl. Nurs. Res.* **18**, 29–35 (2005).
- Sonenblum, S. E., Sprigle, S. H. & Martin, J. S. Everyday sitting behavior of full-time wheelchair users. *J. Rehabil. Res. Dev.* **53**, 585–598 (2016).
- Tavares, C. et al. Wheelchair pressure ulcer prevention using FBG based sensing devices. *Sensors* **20**, 212 (2020).
- Goodwin, B. M. et al. Visualization of user interactions with a pressure mapping mobile application for wheelchair users at risk for pressure injuries. *Assist. Technol.* **34**, 444–453 (2022).
- Oh, Y. S. et al. Battery-free, wireless soft sensors for continuous multi-site measurements of pressure and temperature from patients at risk for pressure injuries. *Nat. Commun.* **12**, 5008 (2021).

26. Han, S. et al. Battery-free, wireless sensors for full-body pressure and temperature mapping. *Sci. Transl. Med.* **10**, eaan4950 (2018).
27. Kwak, J. W. et al. Wireless sensors for continuous, multimodal measurements at the skin interface with lower limb prostheses. *Sci. Transl. Med.* **12**, eabc4327 (2020).
28. Park, Y. et al. Wireless, skin-interfaced sensors for compression therapy. *Sci. Adv.* **6**, eabe1655 (2020).
29. Pham, S. et al. Wearable sensor system to monitor physical activity and the physiological effects of heat exposure. *Sensors* **20**, 855 (2020).
30. Kim, S. et al. Soft, skin-interfaced microfluidic systems with integrated immunoassays, fluorometric sensors, and impedance measurement capabilities. *Proc. Natl Acad. Sci. U. S. A.* **117**, 27906–27915 (2020).
31. Verbunt, M. & Bartneck, C. Sensing senses: Tactile feedback for the prevention of Decubitus ulcers. *Appl. Psychophysiol. Biofeedback* **35**, 243–250 (2010).
32. Dai, R., Sonenblum, S. E. & Sprigle, S. A robust wheelchair pressure relief monitoring system. *Proc. Annu. Int. Conf. IEEE Eng. Med. Biol. Soc. EMBS* **2012**, 6107–6110 (2012).
33. Cui, J., Cui, L., Huang, Z., Li, X. & Han, F. IoT wheelchair control system based on multi-mode sensing and human-machine interaction. *Micromachines* **13**, 1108 (2022).
34. Gakopoulos, S. et al. Development of a data logger for capturing human-machine interaction in wheelchair head-foot steering sensor system in dyskinetic cerebral palsy. *Sensors* **19**, 5404 (2019).
35. Rossignoli, I., Benito, P. J. & Herrero, A. J. Reliability of infrared thermography in skin temperature evaluation of wheelchair users. *Spinal Cord* **53**, 243–248 (2015).
36. Abdur-Rahim, J. et al. Multi-sensor based state prediction for personal mobility vehicles. *PLoS One* **11**, 1–29 (2016).
37. Kang, S. K. et al. Bioresorbable silicon electronic sensors for the brain. *Nature* **530**, 71–76 (2016).
38. Won, S. M. et al. Multimodal sensing with a three-dimensional Piezoresistive structure. *ACS Nano* **13**, 10972–10979 (2019).
39. Shin, J. et al. Bioresorbable pressure sensors protected with thermally grown silicon dioxide for the monitoring of chronic diseases and healing processes. *Nat. Biomed. Eng.* **3**, 37–46 (2019).
40. Gul, O. et al. Sensitivity-controllable liquid-metal-based pressure sensor for wearable applications. *ACS Appl. Electron. Mater.* **3**, 4027–4036 (2021).
41. Gao, Y. et al. Wearable microfluidic diaphragm pressure sensor for health and tactile touch monitoring. *Adv. Mater.* **29**, 1701985 (2017).
42. Jeong, Y. R. et al. A skin-attachable, stretchable integrated system based on liquid GaInSn for wireless human motion monitoring with multi-site sensing capabilities. *NPG Asia Mater.* **9**, e443 (2017).
43. Kim, K. et al. Highly sensitive and wearable liquid metal-based pressure sensor for health monitoring applications: Integration of a 3D-printed microbump array with the microchannel. *Adv. Healthc. Mater.* **8**, 1900978 (2019).
44. Hu, W. et al. Amalgamation-assisted control of profile of liquid metal for the fabrication of microfluidic mixer and wearable pressure sensor. *Adv. Mater. Interfaces* **8**, 2100038 (2021).
45. Tao, L. Q. et al. Graphene-paper pressure sensor for detecting human motions. *ACS Nano* **11**, 8790–8795 (2017).
46. Pang, Y. et al. Epidermis microstructure inspired graphene pressure sensor with random distributed spinosum for high sensitivity and large linearity. *ACS Nano* **12**, 2346–2354 (2018).
47. He, J. et al. A Universal high accuracy wearable pulse monitoring system via high sensitivity and large linearity graphene pressure sensor. *Nano Energy* **59**, 422–433 (2019).
48. Kim, S. et al. Wearable, ultrawide-range, and bending-insensitive pressure sensor based on carbon nanotube network-coated porous elastomer sponges for human interface and healthcare devices. *ACS Appl. Mater. Interfaces* **11**, 23639–23648 (2019).
49. Jeong, Y. et al. Ultra-wide range pressure sensor based on a microstructured conductive nanocomposite for wearable workout monitoring. *Adv. Healthc. Mater.* **10**, 2001461 (2021).
50. Kim, Y. et al. A bioinspired flexible organic artificial afferent nerve. *Science* **360**, 998–1003 (2018).
51. Kang, D. et al. Ultrasensitive mechanical crack-based sensor inspired by the spider sensory system. *Nature* **516**, 222–226 (2014).
52. Park, B. et al. Dramatically enhanced mechanosensitivity and signal-to-noise ratio of nanoscale crack-based sensors: effect of crack depth. *Adv. Mater.* **28**, 8130–8137 (2016).
53. Wang, D. Y. et al. High-performance flexible strain sensor based on self-locked overlapping graphene sheets. *Nanoscale* **8**, 20090–20095 (2016).
54. Kim, T. et al. Polyimide encapsulation of spider-inspired crack-based sensors for durability improvement. *Appl. Sci.* **8**, 367 (2018).
55. Kim, D. S. et al. Highly durable crack sensor integrated with silicone rubber cantilever for measuring cardiac contractility. *Nat. Commun.* **11**, 1–13 (2020).
56. Park, B. et al. A semi-permanent and durable nanoscale-crack-based sensor by on-demand healing. *Nanoscale* **10**, 4354–4360 (2018).
57. Wood, A. D. et al. Bioelectrical impedance versus biochemical analysis of hydration status: Predictive value for prolonged hospitalisation and poor discharge destination for older patients. *Healthcare* **9**, 154 (2021).
58. Pang, C. et al. Highly skin-conformal microhair sensor for pulse signal amplification. *Adv. Mater.* **27**, 634–640 (2015).
59. Hoang, M. V., Chung, H. J. & Elias, A. L. Irreversible bonding of polyimide and polydimethylsiloxane (PDMS) based on a thiol-epoxy click reaction. *J. Microeng. Microeng.* **26**, 105019 (2016).

ACKNOWLEDGEMENTS

S.C., H.H., J.G., C.H., K.L., and I.P. are supported by the Technology Innovation Program (00144157, Development of Heterogeneous Multi-Sensor Micro-System Platform) funded By the Ministry of Trade, Industry & Energy(MOTIE, Korea) and the National Research Foundation of Korea (NRF) grant funded by the Korea government (MSIT) (no. 2021R1A2C3008742). Y.T.C. supported by the MSIT(Ministry of Science and ICT), Korea, under the Grand Information Technology Research Center support program(IITP-2022-2016-0-00318) supervised by the IITP(Institute for Information & communications Technology Planning & Evaluation) Z.X. acknowledges the support from the National Natural Science Foundation of China (Grant No. 12072057).

AUTHOR CONTRIBUTIONS

S.C., Y.S.O., and I.P. led the development of the concepts, designed the experiments, and interpreted results. S.Cho led the experimental work with support from H.H., H.P., J.-H.K., S.W.J., K.K., M.P., J.L., M.C.i, J.-S.L., W.G.M., B.-J.L., J.C., J.G., J.P., M.S.K., J.A., O.G., C.H., G.L., S.K., K.K., J.K., C.-M.K., J.K., S.S.K., S.K., D.Y.C., S.J., H.J.S., Y.T.C., M.J., S.-U.L., S.C., Y.S.O. performed the mechanical modelling and simulations. Z.X., M.W., R.A., S.L., Y.B.P. performed the electromagnetic simulations of the antenna system. S.C., Y.S.O., and I.P. wrote the paper.

COMPETING INTERESTS

The authors declare no competing interests.

ADDITIONAL INFORMATION

Supplementary information The online version contains supplementary material available at <https://doi.org/10.1038/s41528-023-00238-3>.

Correspondence and requests for materials should be addressed to Yong Suk Oh or Inkyu Park.

Reprints and permission information is available at <http://www.nature.com/reprints>

Publisher's note Springer Nature remains neutral with regard to jurisdictional claims in published maps and institutional affiliations.



Open Access This article is licensed under a Creative Commons Attribution 4.0 International License, which permits use, sharing, adaptation, distribution and reproduction in any medium or format, as long as you give appropriate credit to the original author(s) and the source, provide a link to the Creative Commons license, and indicate if changes were made. The images or other third party material in this article are included in the article's Creative Commons license, unless indicated otherwise in a credit line to the material. If material is not included in the article's Creative Commons license and your intended use is not permitted by statutory regulation or exceeds the permitted use, you will need to obtain permission directly from the copyright holder. To view a copy of this license, visit <http://creativecommons.org/licenses/by/4.0/>.

© The Author(s) 2023